PHYSICAL REVIEW B **85**, 235403 (2012)

Measurement of the dynamics of plasmons inside individual gold nanoparticles using a femtosecond phase-resolved microscope

Francesco Masia,[1,2] Wolfgang Langbein,[1] and Paola Borri[1,2,*]

[1] *Cardiff University School of Physics and Astronomy, The Parade, Cardiff CF24 3AA, United Kingdom*

[2] *Cardiff University School of Biosciences, Museum Avenue, Cardiff CF10 3AX, United Kingdom*

(Received 29 February 2012; revised manuscript received 16 April 2012; published 1 June 2012)

We demonstrate a phase-sensitive four-wave mixing microscopy in heterodyne detection to resolve the ultrafast changes of the real and imaginary parts of the dielectric function of single small (<40 nm) spherical gold nanoparticles at the surface plasmon resonance. The results are quantitatively described via the transient electron temperature and density in gold considering both intraband and interband transitions. We find that the effect of interband transitions in the excitation is important to explain not only the magnitude of the measured four-wave mixing, but also its initial dynamics, which is dominated by the formation of hot electrons via Auger electron-hole recombination with 70-fs time constant, much faster than the well-characterized 500-fs electron thermalization dynamics for intraband excitation. This microscopy technique enables background-free detection of the complex susceptibility change even in highly scattering environments and can be readily applied to any metal nanostructure.

DOI: 10.1103/PhysRevB.85.235403 PACS number(s): 78.67.Bf, 78.47.jh, 78.47.nj

I. INTRODUCTION

Metallic nanoparticles (NPs) exhibit morphology-dependent electromagnetic resonances also called surface plasmon resonances (SPR), which couple to propagating light. These resonances originate from a coherent oscillation of electrons in the metal where the restoring force is due to the electric field created by the corresponding charge displacement. Since this electric field depends on the morphology, the SPR frequency and linewidth is a function of the shape and size of the NP and its dielectric environment.[1–3] The resulting local optical resonances can be exploited to image metallic NPs with high spatial resolution and to probe nanoscale regions in the NP vicinity through the local electric field of the resonance. In particular, gold NPs are ideal optical labels for biological applications owing to their biocompatibility and photostability, and much effort has been devoted recently to develop techniques capable of detecting gold NPs in cells and tissues with high contrast and sensitivity to the single-particle level.[4–9]

Ultrafast optical spectroscopy of metallic NPs is an intriguing area of research investigating the correlated electronic and vibrational dynamics in nanosized metals. Due to limited detection sensitivity, most of the experiments performed so far[10,11] used large ensembles of metallic NPs, with the associated difficulty of inhomogeneous NP size, shape, and environment fluctuations. Only few reports on ultrafast pump-probe spectroscopy on single small metallic NPs (Refs. 11–14) are available to date. Importantly, these experiments lacked the ability to extract the change in the NP dielectric function as a *complex* quantity separating its real and imaginary parts.[15] This, however, is the key physical quantity of interest, being a function of the electron and lattice temperatures transiently changing in the thermalization dynamics.[10]

To overcome these limitations, in this work we demonstrate a phase-sensitive four-wave mixing (FWM) microscopy technique in heterodyne detection with which we resolve the ultrafast changes of real and imaginary parts of the dielectric function of single spherical gold NPs with diameters between 15 and 40 nm. To quantitatively explain the experimental results, we also developed a consistent model with which we describe the ultrafast changes of the real and imaginary parts of the dielectric function in terms of the transient electron temperature and density in gold considering both intraband and interband transitions at the SPR.

II. EXPERIMENTAL SETUP

A sketch of the experimental setup is shown in Fig. 1. Optical pulses are provided by the intracavity frequency doubled signal of an optical parametric oscillator (APE-PP2) pumped by a femtosecond Ti:sapphire oscillator (Coherent Mira) of $\nu_L = 76.1$ MHz repetition rate. We used pulses with a tunable center wavelength from 540 to 590 nm and a Fourier-limited duration ranging from 150 to 180 fs (intensity full width at half-maximum) depending on the wavelength (corresponding to 2.5 nm spectral width at 550 nm). The pulse train at the output of the optical parametric oscillator is split into three beams having all the same center wavelength (degenerate FWM scheme). One beam acts as pump and excites the NP with an intensity which is temporally modulated with close to unity depth by an acousto-optic modulator (AOM) driven with a square wave amplitude modulation of frequency $\nu_m = 1$ MHz. This implementation replaces the two-beam interference used in our previous work,[9] providing a stable phase of the modulation. The change in the NP optical properties induced by this excitation is probed by a second pulse at an adjustable delay time τ after the pump pulse. The delay times between the pulses are controlled with 10-fs accuracy by linear stages. Pump and probe pulses of fields E_1 and E_2, respectively, are recombined into the same spatial mode and focused onto the sample by an oil-immersion microscope objective (MO) of 1.25 numerical aperture (NA) to achieve high spatial resolution. The sample is positioned with respect to the focal volume of the objective by an xyz piezoelectric stage with 10-nm resolution (Physik Instrumente Nanocube). A FWM signal proportional to $E_1 E_1^* E_2$ is collected in transmission by a second identical MO, recombined in a beam splitter with a reference pulse of adjustable delay, and the resulting

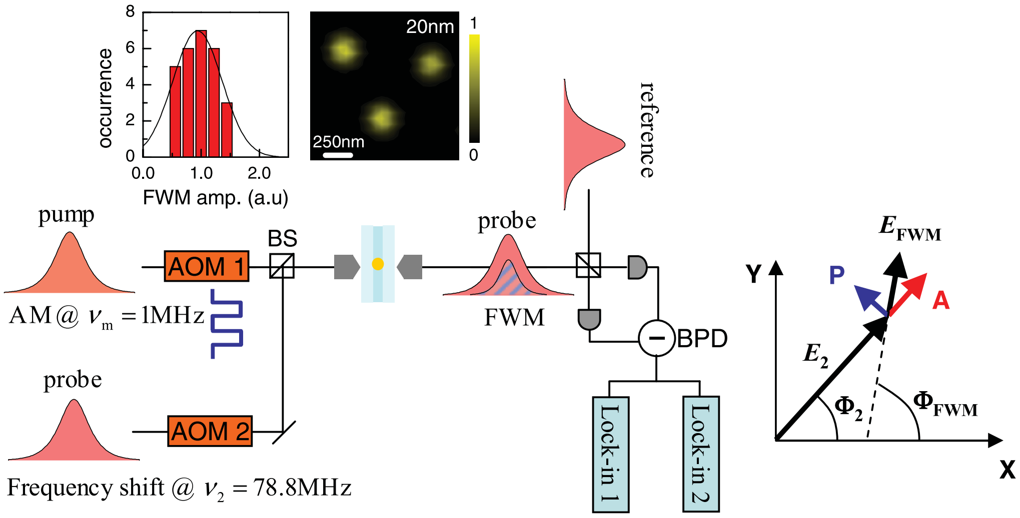

FIG. 1. (Color online) Sketch of the phase-resolved transient FWM microspectroscopy technique (see text). AOM: acousto-optics modulator; BS: 50:50 beam splitter; BPD: balanced photodiodes. Top inset: FWM imaging of 20-nm gold NPs resonantly excited and probed at 550 nm and corresponding histogram with a Gaussian fit showing a monomodal size distribution (the deduced relative size distribution is 30%). Right: Sketch of the phase-resolved detection using two dual-channel lock-in amplifiers to measure the X and Y components of the probe field E_2 and FWM field E_{FWM}.

interference is detected by balanced silicon photodiodes (for common-mode noise rejection) and a dual-channel lock-in amplifier (SRS SR844). We used a heterodyne scheme to discriminate the FWM field from pump and probe pulses and to detect amplitude and phase of the field. By upshifting the probe optical frequency via a second AOM (driven with a constant amplitude at a frequency of $\nu_2 = 78.8$ MHz), we detected the interference of the FWM with the unshifted reference field. This interference gives rise to a beat note at the radiofrequency $\nu_2 - \nu_{\mathrm{m}}$ and its sidebands separated by the repetition rate ν_{L} of the pulse train. We detect at the radiofrequency sideband $\nu_2 - \nu_{\mathrm{m}} - \nu_{\mathrm{L}} = 1.7$ MHz with the lock-in amplifier by creating an electric signal for the lock-in reference channel, which is synchronized with the optical interference (via appropriate mixing of electric outputs from the AOM drivers and the laser at the AOM radiofrequencies and laser repetition rate[16]). We simultaneously detect the interference of the transmitted probe with the reference field at $\nu_2 - \nu_{\mathrm{L}} = 2.7$ MHz using a second dual-channel lock-in electronically referenced at this frequency, and deduce the amplitude (A) and phase (P) components of the FWM field relative to the transmitted probe as follows (see also sketch in Fig. 1). The dual-channel lock-in amplifiers measure the X and Y components of E_2 and E_{FWM}. We define the amplitude part A as the projection of E_{FWM} onto E_2 and the phase part P as its orthogonal component via the expressions $A = (X_2X_{\mathrm{FWM}} + Y_2Y_{\mathrm{FWM}})/|E_2|^2$ and $P = (X_2Y_{\mathrm{FWM}} - Y_2X_{\mathrm{FWM}})/|E_2|^2$. We calibrate the relative phase offset of the two lock-in amplifiers using a known amplitude and phase modulation of the probe. For this purpose, we measure an electrically pumped quantum-dot optical amplifier, which shows pump-induced changes of the gain and refractive index[17] resulting in large changes of amplitude (>10%) and phase (>10°) of the transmitted probe field. These changes can be measured with the FWM experiment, but also directly by measuring X_2 and Y_2 with and without the pump using a slow (5-Hz) modulation. Both measurements have to yield the same result since the response of the optical amplifier is the same at 1 MHz and 5 Hz. This requirement determines the phase offset ϕ_{o} between the two lock-in amplifiers in the FWM experiment, which is taken into account by transforming the values $X_2^{(M)}$, $Y_2^{(M)}$ directly measured by the lock-in into $X_2 = X_2^{(M)}\cos(\phi_{\mathrm{o}}) - Y_2^{(M)}\sin(\phi_{\mathrm{o}})$, $Y_2 = Y_2^{(M)}\cos(\phi_{\mathrm{o}}) + X_2^{(M)}\sin(\phi_{\mathrm{o}})$. The phase offset reproducibility during the course of the experiments was found to be a few degrees (corresponding to a few nanoseconds delay), as expected from the rf electronics used to create the lock-in reference signals.

We also employed a cross-polarization scheme to reject background originating from noninearities of the photodiodes, in which the polarization state of E_1 was adjusted by a combination of $\lambda/4$ and $\lambda/2$ waveplates to be cross-linearly polarized to E_2 and the reference beam. Polarizers in front of the photodiodes transmit the FWM, E_2, and reference fields, but block the pump field E_1.

In this work, samples were prepared using commercially available gold NPs in aqueous suspension (BB International) drop cast on a glass cover slip at sufficiently low density so that regions with well-separated individual NPs were formed, and subsequently embedded in a mounting medium (Cargille Meltmount) index-matched to the oil-immersion microscope objectives used for high-resolution imaging.

We have previously demonstrated background-free FWM imaging in a highly scattering and fluorescing environment, and sensitivity to the single NP level with a spatial resolution significantly surpassing one photon diffraction.[9] An example of FWM imaging of gold NPs of 20 nm diameter resonantly excited and probed at 550 nm is shown in the inset of Fig. 1 together with a histogram indicating a monomodal size distribution well separated from the noise level (here, ∼1/100 of the NP signal), confirming that each spot is a single NP.

III. ULTRAFAST DYNAMICS OF THE COMPLEX DIELECTRIC FUNCTION

To explain how the detection of A and P enables us to distinguish the transient changes of the real and imaginary parts of the dielectric function of a single NP, we write the induced polarization field at the particle as $p = \epsilon_0 \epsilon_d \alpha E_2$, where ϵ_0 is the vacuum permittivity, ϵ_d is the dielectric constant of the medium surrounding the NP, and α is the particle polarizability. For a particle radius R much smaller than the wavelength of light (Rayleigh limit), the polarizability is given by

$$\alpha = 4\pi R^3 \frac{\epsilon - \epsilon_d}{\epsilon + 2\epsilon_d} \equiv 4\pi R^3 \widetilde{\epsilon} \tag{1}$$

with the particle dielectric constant ϵ defining an effective dielectric constant $\widetilde{\epsilon}$. The pump-induced change of $\widetilde{\epsilon}$, denoted as $\Delta\widetilde{\epsilon}$, creates the FWM field proportional to the change of polarization, i.e., $E_{\rm FWM} \propto \Delta\widetilde{\epsilon} E_2$. The complex dielectric constant is then expressed in terms of its amplitude and phase $\Delta\widetilde{\epsilon} = |\Delta\widetilde{\epsilon}| \exp(i\varphi) = \Delta\widetilde{\epsilon}_R + i\Delta\widetilde{\epsilon}_I$, as well as the probe field $E_2 = |E_2| \exp(i\phi)$, such that $E_{\rm FWM} \propto |\Delta\widetilde{\epsilon}||E_2| \exp[i(\phi + \varphi)]$. Hence, φ is the phase difference between the FWM field and the probe field at the particle position. The transmitted probe in the far field acquires a phase shift compared to a spherical wave of the FWM field, known as Gouy phase shift for a Gaussian beam. The Gouy phase shift is $-\pi/2$ from the focus to infinity, hence, in the far field the FWM field is phase shifted relative to the transmitted probe by $\varphi + \pi/2$. The amplitude modulation of the transmitted probe is then (see sketch in Fig. 1) $A \propto |\Delta\widetilde{\epsilon}| \cos(\varphi + \pi/2) = -|\Delta\widetilde{\epsilon}| \sin(\varphi) = -\Delta\widetilde{\epsilon}_I$ and the phase modulation is $P \propto |\Delta\widetilde{\epsilon}| \sin(\varphi + \pi/2) = |\Delta\widetilde{\epsilon}| \cos(\varphi) = \Delta\widetilde{\epsilon}_R$. Note that the particle absorption cross section is proportional to the imaginary part of α as can be deduced from Mie theory in the small-particle limit, hence, A is a measure of the change in absorption cross section.

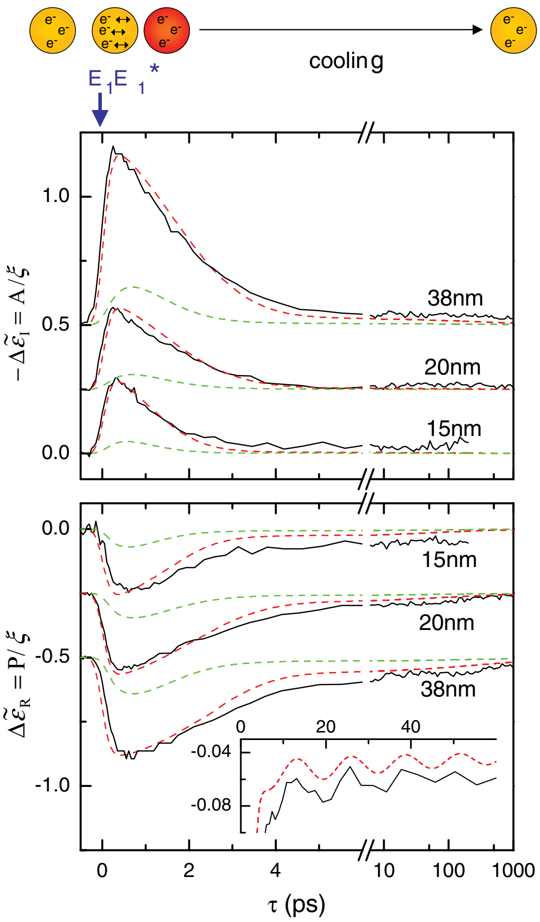

FIG. 2. (Color online) Transient changes of the real ($\Delta\widetilde{\epsilon}_R$) and imaginary ($\Delta\widetilde{\epsilon}_I$) parts of the dielectric function of a single gold NP resonantly excited and probed at 550 nm for different NP diameters as indicated. Pump (probe) fluence is 0.60 J/m^2 (0.11 J/m^2) for the 15- and 20-nm NPs and 0.65 J/m^2 (0.05 J/m^2) for the 38-nm particle. Acquisition time per point is 200 ms. Dashed lines are corresponding calculations (see text), with the green lines neglecting the heating by interband absorption. Curves are vertically displaced for clarity. The top sketch illustrates the SPR excitation by the pump (E_1) and the subsequent heating and cooling dynamics monitored by the probe. The inset shows coherent phonon oscillations for the 38-nm NP.

The measured A and P versus pump-probe delay for single gold NPs of various sizes resonantly excited and probed at 550 nm are shown in Fig. 2. Both exhibit an initial dynamics in the picosecond time scale followed by a decay in the hundreds of picoseconds. Qualitatively, one can understand these dynamics as being related to the pump-induced increase in the electron temperature which provokes a broadening and a shift of the SPR probed by E_2. The picosecond decay is related to the thermalization of the hot electron gas with the cooler lattice by electron-phonon coupling, while the thermalization of the heated NP with the cooler surrounding is providing the subsequent decay. For a quantitative description of the measured dynamics, we modeled $\widetilde{\epsilon}$ using the gold NP dielectric function

$$\epsilon = 1 - \frac{\omega_p^2}{\omega(\omega + i\Gamma)} + \epsilon^b(\omega), \tag{2}$$

where $\omega_p^2 = n_e e^2/\epsilon_0 m_0$ is the plasma frequency (n_e, e, and m_0 being the conduction electron density, charge, and effective mass, respectively), Γ is the electron relaxation rate, and ϵ^b is the contribution due to bound electrons associated with interband transitions from the d bands to the conduction band. At room temperature in the absence of optical excitation, Γ can be approximated as[18]

$$\Gamma_0 = \gamma_0 + g\frac{v_F}{R}, \tag{3}$$

where γ_0 is the bulk damping rate, $v_F = 1.4 \times 10^6$ m/s is the Fermi velocity, and g parametrizes surface damping effects. For bulk gold, we used $\hbar\omega_p = 9$ eV and $\hbar\gamma_0 = 70$ meV, well reproducing the Drude part of the bulk dielectric constant measured by Johnson and Christy.[19] These values also reproduce experimental absorption spectra of single gold nanoparticles in the literature.[2] The parameter g varies in the literature[2,3] from 0.2 to 2.2, and even between individual NPs within the same experiment. This variance is likely to be related to the atomistic NP surface structure/faceting,[3] hence we use g as free parameter falling in the range of previously reported values. In the presence of optical excitation, we then model the change in the electron temperature T_e and lattice temperature T_l using a two-temperature model[12,18] (see Appendix A2)

$$C_e(T_e)\frac{dT_e}{dt} = -G_{e\text{-}p}(T_e - T_l) + P(t), \tag{4}$$

$$C_l\frac{dT_l}{dt} = G_{e\text{-}p}(T_e - T_l) - \dot{Q}, \tag{5}$$

where C_e is the electronic heat capacity, well described by $C_e = \gamma T_e$ for[20] $T_e < 3000$ K, C_l is the lattice heat capacity, and $G_{e\text{-}p}$ is the electron-phonon coupling constant. C_e and C_l are taken as the bulk value scaled to the NP volume. $\dot{Q}$ is the heat transfer rate from the particle to the surrounding and is calculated using the diffusion equation for the temperature of the surrounding medium. $P(t)$ is the heating power of the excitation, which has two components P_f and P_b related to free and bound electrons, respectively. The bound-electron contribution has to be considered since in spherical gold NPs, the onset of interband transitions from d bands to the conduction band at the Fermi surface is energetically close to the SPR.[18] P_f is modeled as a rapid (∼10 fs, quasi-instantaneous for the 150-fs pulses used) transfer of energy from the resonantly excited SPR to single-electron excitations of the conduction band, which thermalize with the free-electron gas creating a hot Fermi-Dirac distribution on a characteristic time scale τ_f.[10,18] Similarly, P_b originates from the transfer of energy from the SPR to interband excitations and consequent heating of the free-electron gas via Auger electron-hole recombination with a characteristic time τ_b. Noticeably, most pump-probe experiments in previous literature use a pump photon energy below the onset of interband transitions, and thus neglect the latter effect.[10,11] The time integral of $P(t)$ is equal to the absorbed energy calculated from the NP absorption cross section and the pump-pulse fluence in the experiment. More details are given in Appendix A1.

The nonequilibrium electron and lattice temperatures modify the electron-electron and electron-phonon scattering processes, which can be described[21] by $\Gamma = \Gamma_0 + \gamma_{e\text{-}p} + \gamma_{e\text{-}e}$ with

$$\gamma_{e\text{-}p}(T_l) = b_{e\text{-}p}\hbar^2\omega^2(T_l - T_0), \tag{6}$$

and

$$\gamma_{e\text{-}e}(T_e) = b_{e\text{-}e}\hbar^2\omega^2\left(T_e^2 - T_0^2\right) \tag{7}$$

using the equilibrium temperature T_0. The electron and lattice temperatures also affect ϵ^b. To estimate this effect, we calculated the imaginary part ϵ_2^b of ϵ^b due to interband transitions near the X and L points, starting from the description in Refs. 22 and 23. The temperature dependence of ϵ^b results from the Fermi distribution and a spectral broadening proportional to Γ (see Appendix A3). The real part of ϵ^b is calculated from ϵ_2^b using Kramers-Kronig relations.

The transient change in ϵ modifies $\tilde{\epsilon}$ and is the source of the measured $\Delta\tilde{\epsilon}_I$ and $\Delta\tilde{\epsilon}_R$ via $A = -\xi\Delta\tilde{\epsilon}_I$ and $P = \xi\Delta\tilde{\epsilon}_R$ with a constant ξ.[24] We are able to consistently model all measured dynamics for particle sizes up to 40 nm diameter and for different pump excitation intensities in the 0.12–1.3 J/m^2 range with only few particle-dependent (g, $G_{e\text{-}p}$) and particle-independent ($b_{e\text{-}e}$, $b_{e\text{-}p}$, τ_f, τ_b) parameters. Measurements and calculations are shown in Fig. 2 for different particle sizes and in Fig. 3 for different pump excitation intensities. The gold band-structure parameters to calculate ϵ^b are taken from literature.[22,23] The proportionality term ξ scales with R^3 and is independent of the pump intensity as expected from the particle polarizability α. Larger particles have a polarizability, which deviates significantly from the Rayleigh limit used here, and we found that FWM dynamics measured on >100-nm diameter particles can no longer be described by our model (see Appendix B). We calibrated the size of the 38-nm NP investigated in Fig. 2 using the period of the coherent phonon oscillations observed in $\Delta\tilde{\epsilon}_R$ (see inset in Fig. 2). These are due to the modulation of the plasma frequency by the breathing vibrational mode of the NP with an oscillation period proportional to the particle radius[11,13,18] (see Appendix C). On NPs smaller than 20 nm, the oscillation period was not resolved, possibly because its time scale becomes comparable to the lattice expansion, which is no longer impulsively exciting the vibrational mode and its amplitude falls below the measurement noise. In this case, the particle size was derived from the strength of the measured FWM field relative to that of the 38-nm particle, consistently with $\xi \propto R^3$.

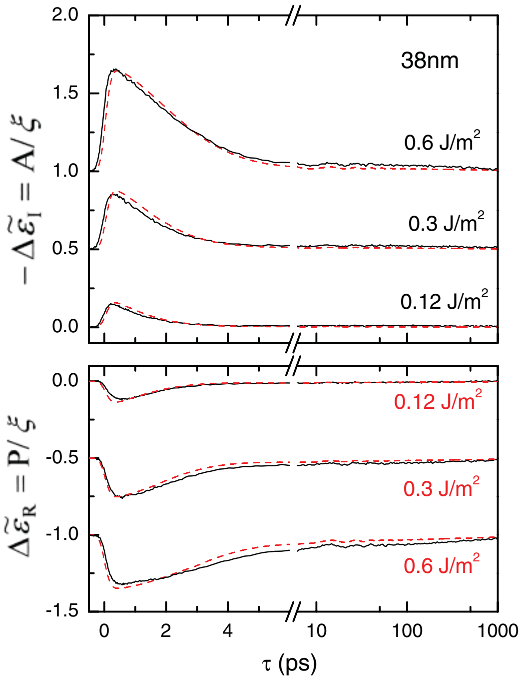

FIG. 3. (Color online) Transient changes of the real ($\Delta\tilde{\epsilon}_R$) and imaginary ($\Delta\tilde{\epsilon}_I$) parts of the dielectric function of a single gold NP resonantly excited and probed at 550 nm for different pump excitation intensities as indicated. Probe fluence is 0.1 J/m^2. Dashed lines are corresponding calculations (see text). Curves are vertically displaced for clarity.

We use $\tau_f = 500$ fs independent on particle size in the 15–40-nm diameter range from Ref. 18, $b_{e\text{-}e} = 0.89 \times 10^7$ s^{-1} eV^{-2} K^{-2} and $b_{e\text{-}p} = 0.5 \times 10^{11}$ s^{-1} eV^{-2} K^{-1} consistent with Ref. 21, and g in the range 1.8–1.9 consistent with Ref. 3.

The fast rise of $\Delta\tilde{\epsilon}_I$ and $\Delta\tilde{\epsilon}_R$ observed in our data reveals a fast d-state Auger recombination time of $\tau_b = 70$ fs $\ll \tau_f$. While this time has not been measured previously in Au, it is within the energy-dependent range of 250–20 fs measured in Cu.[25] To clarify the significance of interband transitions in the SPR resonant excitation, we show in Fig. 2 simulations

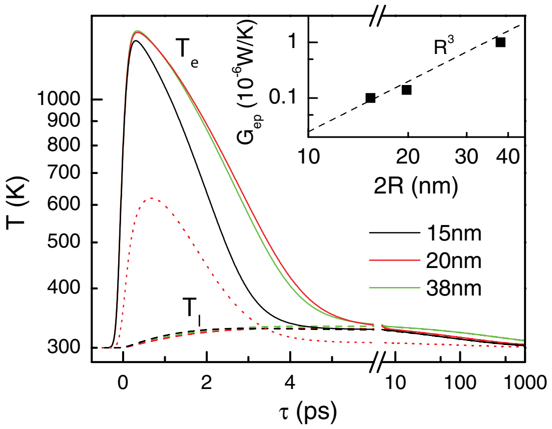

FIG. 4. (Color online) Transients of the electron temperature (solid lines) and lattice temperature (dashed lines) for different NP sizes as indicated, calculated for a pump fluence of 0.60 J/m^2. The dotted curve is the electron temperature of a 20-nm NP when the excitation term involving bound electrons is neglected. The inset shows the electron-phonon coupling parameter used in the calculations. The dashed line in the inset indicates the volumetric scaling.

(green lines) neglecting the heating P_b. The effect of interband transitions in the excitation is important to account not only for the magnitude of the measured change, but also its dynamics, particularly for the observed fast rise time. We could simulate the measured rise time without the interband contribution only when using $\tau_f < 100$ fs, much faster than the well-characterized 500-fs electron thermalization dynamics[18] in bulk gold and gold NPs larger than 10 nm. The faster Auger recombination of the d holes can be attributed to a higher density of states available in the scattering involving the lower-lying d states.

It is instructive to examine the temperature transients of T_e and T_l, which are shown in Fig. 4. Noticeably, the electron temperature reaches a maximum value which is almost independent of NP size. This is a consequence of the volumetric dependence of both the electron heat capacity and the absorption cross section, compensating each other. The decay of T_e on the picosecond time scale coincides with the rise of T_l due to electron-phonon coupling, and the electron temperature after thermalization is much lower due to the significantly larger lattice heat capacity ($C_l \gg C_e$). We find that $G_{e\text{-}p}$ also has a nearly volumetric dependence, and in turn the electron-phonon dynamics exhibits only a weak size dependence in the size range 15–40 nm investigated here, consistent with reports in the literature.[26] By analyzing the cooling dynamics to the lattice, we have verified that energy transfer between electron and lattice is proportional to their temperature difference, as assumed in the two-temperature model (see Appendix D).

We also observe that the cooling with the environment is size dependent, with smaller particles cooling faster.[11] We point out that the *average* temperature increase at the particle surface is only 1.3, 1.9, and 4.7 K for 15, 20, and 38 nm diameters, respectively, and can be lowered to 0.9 K for 38 nm diameter at the lowest (0.12 J/m^2) pump excitation used in the experiment. Importantly, such low average photothermal heating indicates that our technique is compatible with live cell applications. Finally, the effect of P_b is shown by plotting T_e in its absence (dotted curve in Fig. 4), which shows a delayed rise and reaches only about half of the maximum electron temperature.

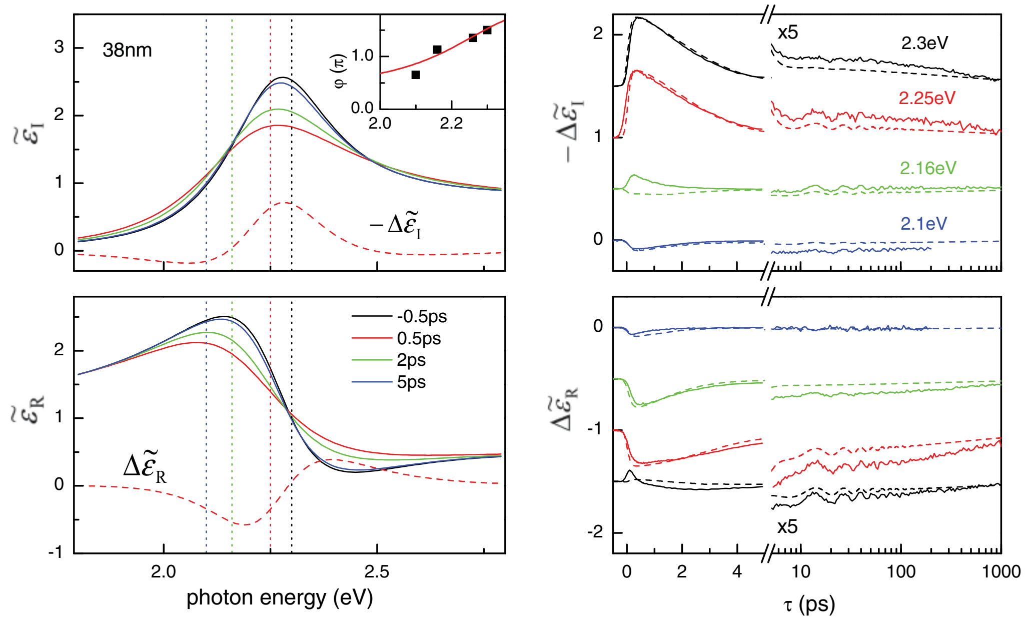

FIG. 5. (Color online) Left: Spectrally resolved real and imaginary parts of the dielectric constant $\tilde{\epsilon}$ simulated for the 38-nm NP at various delay times for an excitation at 550 nm. Dashed lines are the differential spectra at $\tau = 0.5$ ps. Vertical dotted lines indicate the excitation and detection photon energies used in the experiment on the right. In the inset, the phase of $\Delta\tilde{\epsilon}$ is shown at $\tau = 0.5$ ps (symbols: experiment; line: simulation). Right: Measurement and simulations of the transient changes of the real and imaginary parts of the dielectric function at different photon energies, as indicated. The pump fluence was 0.48 J/m^2 at 540 nm and 0.6 J/m^2 for all other wavelengths. Curves are vertically displaced for clarity.

To visualize the origin of the FWM signal in terms of broadening and shift of the SPR, we plot in Fig. 5 the spectra of $\widetilde{\epsilon}_\mathrm{I}$ and $\widetilde{\epsilon}_\mathrm{R}$ at different delay times for an excitation at 550 nm. The negative change of $\widetilde{\epsilon}_\mathrm{I}$ probed at 550 nm (see dotted red vertical line in Fig. 5) is mainly a result of the broadening of the SPR and in turn quenching of the resonance. Conversely, the negative change of $\widetilde{\epsilon}_\mathrm{R}$ at 550 nm is a combination of the SPR broadening and its frequency shift toward lower energies. Measurements and simulations of $\Delta\widetilde{\epsilon}_\mathrm{I}$ and $\Delta\widetilde{\epsilon}_\mathrm{R}$ excited and probed at 540 nm ($\hbar\omega = 2.3$ eV) and 575 nm ($\hbar\omega = 2.16$ eV) elucidate the cases of $\Delta\widetilde{\epsilon}_\mathrm{I}$ being mostly sensitive to the SPR broadening and $\Delta\widetilde{\epsilon}_\mathrm{R}$ to the SPR shift, and vice versa. Specifically, we see that at 2.3 eV, $\Delta\widetilde{\epsilon}_\mathrm{R}$ is a sensitive probe of the modulation of the SPR by the breathing vibrational mode, while $\Delta\widetilde{\epsilon}_\mathrm{I}$ is essentially unaffected by it. We also performed measurements and simulations at 590 nm ($\hbar\omega = 2.10$ eV) where $\Delta\widetilde{\epsilon}_\mathrm{I}$ changes sign. Noticeably, the initial dynamics measured at different wavelengths is consistently reproduced by our model of the fast Auger recombination of the d holes. Finally, to illustrate that the imaging technique presented here can be used to sense SPR shifts relative to the probe wavelength in an intrinsic ratiometric way independent of the signal strength, we show in the inset of Fig. 5 the phase φ of $\Delta\widetilde{\epsilon} = |\Delta\widetilde{\epsilon}| \exp(i\varphi)$ from the ratio between its imaginary and real parts at $\tau = 0.5$ ps. φ changes by nearly 180° over only 50 nm wavelength as a direct manifestation of the transition from $\Delta\widetilde{\epsilon}_\mathrm{R} = 0$, $\Delta\widetilde{\epsilon}_\mathrm{I} < 0$ ($\varphi = 3\pi/2$, at 540 nm) to $\Delta\widetilde{\epsilon}_\mathrm{I} = 0$, $\Delta\widetilde{\epsilon}_\mathrm{R} < 0$ ($\varphi = \pi$, at 575 nm), to $\Delta\widetilde{\epsilon}_\mathrm{I} > 0$, $\Delta\widetilde{\epsilon}_\mathrm{R} < 0$ ($\pi/2 < \varphi < \pi$, at 590 nm). The dynamics in ratiometric detection is discussed in Appendix E.

IV. SUMMARY

In conclusion, we have demonstrated a phase-sensitive four-wave mixing microscopy in heterodyne detection triply resonant to the SPR of single spherical gold NPs with diameters between 15 and 38 nm. The technique enabled us to resolve the ultrafast changes of real and imaginary parts of the dielectric function of these small NPs. The results agree well with a quantitative model of the FWM response, which accounts for the transient electron temperature and density in gold via intraband and interband transitions at the SPR. Remarkably, we find that the effect of interband transitions in the excitation is important to explain not only the magnitude of the measured FWM, but also its initial dynamics, which is dominated by the formation of hot electrons via Auger electron-hole recombination with 70-fs time constant, much faster than the well-characterized 500-fs electron thermalization dynamics for intraband excitation.

Beyond fundamental interest, our FWM technique offers background-free detection of the full complex susceptibility change even in a highly scattering environment and operates at power levels corresponding to negligible average photothermal heating, hence is compatible with live cell applications. Moreover, it can be readily applied to any NP shape to reveal new physics insights in the electron and lattice dynamics of metallic nanostructures. The intrinsic ratiometric readout in the signal phase demonstrated here has the potential to bring unprecedented sensitivity in SPR-based sensing applications, for example, monitoring nanoscale distance changes with plasmon rulers[27] in cells and tissues.

ACKNOWLEDGMENTS

P.B. acknowledges the EPSRC UK Research Council for her Leadership fellowship award (Grant No. EP/I005072/1). F.M. acknowledges the European Union (Marie Curie Grant Agreement No. PERG08-GA-2010-276807).

APPENDIX A: MODEL OF THE RESPONSE

1. Excitation

The total energy absorbed by the NP is given by $F\sigma_\mathrm{abs}$, where F is the pump-pulse fluence and σ_abs is the NP absorption cross section. It is distributed among the different single-particle excitations (SPE) related to the free-electron gas (SPE $= f$) and the interband transitions involving the X and L points (SPE $= X,L$) respectively. The fraction absorbed by the corresponding SPE is given by the relative contribution f_SPE to the imaginary part of the bulk dielectric constant of the NP $\epsilon_2(\omega_\mathrm{exc})$ at the excitation frequency ω_exc:

$$f_\mathrm{SPE} = \frac{\epsilon_2^\mathrm{SPE}(\omega_\mathrm{exc})}{\epsilon_2(\omega_\mathrm{exc})}, \tag{A1}$$

where ϵ_2^SPE is the contribution in ϵ_2 related to the SPE.

The SPR lifetimes are typically in the ~10-fs range and can be neglected compared to the pulse duration used in our experiments. Assuming a Gaussian temporal intensity profile of the pump pulse

$$I(t) = \frac{F}{\sqrt{\pi\sigma^2}} \exp(-t^2/\sigma^2), \tag{A2}$$

and a subsequent thermalization described as a Markovian process with time constant τ_SPE, the heating power due to the SPE is given by

$$P_\mathrm{SPE}(t) = \frac{F\sigma_\mathrm{abs} f_\mathrm{SPE}}{2\tau_\mathrm{SPE}} \left[1 + \mathrm{erf}\left(\frac{2t\tau_\mathrm{SPE} - \sigma^2}{2\tau_\mathrm{SPE}\sigma}\right)\right] \times \exp\left(\frac{\sigma^2 - 4t\tau_\mathrm{SPE}}{4\tau_\mathrm{SPE}^2}\right), \tag{A3}$$

where σ is given by the pulse duration in the experiment measured for every wavelength (e.g., $\sigma = 0.11$ ps for an intensity full width at half-maximum of 0.18 ps).

We emphasize that the dynamics from a single-particle excitation to a thermalized electron distribution by cascaded electron-electron scattering processes is nontrivial and depends on the electronic band structure and the initial single-particle excitation. It is thus expected that different initial single-particle excitations are described by different effective thermalization times τ_SPE.

P_f originates from the intraband absorption of the free-electron gas and has been described in the literature extensively, having a thermalization time $\tau_\mathrm{f} \approx 500$ fs. $P_\mathrm{b} = P_X + P_L$ instead originates from the absorption of the SPR by interband transitions and consequent Auger electron-hole recombination and heating of the free-electron gas, which we model with a separate thermalization time $\tau_\mathrm{b} = \tau_L = \tau_X$.

To calculate the transient hole densities which influence the dielectric response, we express

$$P_{\mathrm{b}}(t) = \left[n_X^{\mathrm{nth}}(t) + n_L^{\mathrm{nth}}(t)\right]\frac{V\hbar\omega_{\mathrm{exc}}}{\tau_{\mathrm{b}}} \tag{A4}$$

in terms of the densities of photoexcited holes $n_X^{\mathrm{nth}}, n_L^{\mathrm{nth}}$ near the X and L points, respectively, which lead to Auger recombination heating of the electron distribution. Here, V is the particle volume. The densities evolve according to

$$\frac{dn_{X,L}^{\mathrm{nth}}}{dt} = \frac{n_{X,L}}{\sqrt{\pi\sigma^2}}\exp\left(-\frac{t^2}{\sigma^2}\right) - \frac{n_{X,L}^{\mathrm{nth}}}{\tau_{\mathrm{b}}}, \tag{A5}$$

which represents the generation by the Gaussian pulse excitation and the decay due to Auger recombination. The photogenerated densities $n_{X,L}$ are given by

$$n_{X,L} = \frac{F\sigma_{\mathrm{abs}} f_{X,L}}{V\hbar\omega_{\mathrm{exc}}}. \tag{A6}$$

At the resonant excitation wavelength of 550 nm in our experiment, we find $f_X = 0.59$ and $f_L = 0.16$, i.e., 75% of the excitation is absorbed by interband processes. This corresponds for a 38-nm diameter NP with a pump fluence of $F = 0.32$ J/m^2 to photogenerated hole densities of $n_X = 3 \times 10^{-3} n_{\mathrm{e}}$, $n_L = 8 \times 10^{-4} n_{\mathrm{e}}$, with the free-electron density $n_{\mathrm{e}} = 5.9 \times 10^{28}$ m^{-3}. For the other excitation wavelengths used, we find $f_X = 0.57$ and $f_L = 0.24$ at 540 nm, $f_X = 0.59$ and $f_L = 0.09$ at 575 nm, and $f_X = 0.57$ and $f_L = 0.06$ at 590 nm.

2. Two-temperature model

To describe the energy exchange between the optical excitation, electrons in the NP, and lattice, we use a two-temperature model including heat diffusion with the infinitely extended surrounding medium [28,29]

$$C_{\mathrm{e}}\frac{dT_{\mathrm{e}}}{dt} = -G_{\text{e-p}}(T_{\mathrm{e}} - T_{\mathrm{l}}) + P_{\mathrm{f}}(t) + P_{\mathrm{b}}(t), \tag{A7}$$

$$C_{\mathrm{l}}\frac{dT_{\mathrm{l}}}{dt} = G_{\text{e-p}}(T_{\mathrm{e}} - T_{\mathrm{l}}) + 4\pi R^2\kappa_{\mathrm{s}}\left.\frac{\partial T_{\mathrm{s}}}{\partial r}\right|_{r=R}, \tag{A8}$$

$$\frac{\partial T_{\mathrm{s}}}{\partial t} = D_{\mathrm{s}}\frac{1}{r^2}\frac{\partial}{\partial r}\left[r^2\frac{\partial T_{\mathrm{s}}}{\partial r}\right], \tag{A9}$$

where $C_{\mathrm{e}} = \gamma T_{\mathrm{e}}$ is the temperature-dependent electronic heat capacity, C_{l} is the lattice heat capacity, and $G_{\text{e-p}}$ is the electron-phonon coupling constant. We use $\gamma/V = 67.6$ Jm^{-3} K^{-2} and $C_{\mathrm{l}}/V = 2.49 \times 10^6$ Jm^{-3} K^{-1} according to literature, [28,29] and calculate γ for each particle by multiplying with the particle volume $V = \frac{4}{3}\pi R^3$. $T_{\mathrm{s}}(r,t)$ is the temperature of the surrounding which obeys the radial heat diffusion equation (A9), $\kappa_{\mathrm{s}} = 0.07$ Wm^{-1} K^{-1} is the thermal conductivity, and $D_{\mathrm{s}} = 0.1 \times 10^{-7}$ m^2 s^{-1} is the thermal diffusivity of the surrounding. Those values are obtained from the best fit to the FWM dynamics. The thermal conductivity and diffusivity of the mounting medium surrounding the nanoparticles in our experiment (Cargille Meltmount) are not known, but the fitted values are similar to the known values of PVC and epoxy resins. The initial and boundary conditions are as follows: electrons, lattice, and surrounding medium are initially at thermal equilibrium, i.e., $T_{\mathrm{e}}(0) = T_{\mathrm{l}}(0) = T_{\mathrm{s}}(r,0) = T_0 = 300$ K. The surrounding medium in contact with the particle surface and the metal lattice are in thermal equilibrium, $T_{\mathrm{l}}(t) = T_{\mathrm{s}}(R,t)$.

The system of differential equations was solved in MATLAB using the function *pdepe*, which solves initial-boundary value problems for parabolic-elliptic partial differential equations in one dimension.

3. Contribution of interband transitions to the bulk dielectric constant

To calculate ϵ_2^{b}, we use the approach developed in Refs. 22 and 23. We write ϵ_2^{b} in terms of the joint density of states [Eq. (9) in Ref. 22]

$$\epsilon_2^{\mathrm{b}} = \frac{A_X J_X + A_{L^+_{5+6}} J_{L^+_{5+6}} + A_{L^+_4} J_{L^+_4}}{\hbar\omega^2}, \tag{A10}$$

where A_X is proportional to the square of the transition dipole matrix element P_X of the interband transition from the d band to the Fermi surface near the X point of the band structure. Similarly, $A_{L^+_{5+6}}$ and $A_{L^+_4}$ are proportional to the square of the transition dipole matrix elements near the L point, involving the $5+6$ and 4 d bands, respectively (see band structure calculated in Ref. 30). J_X, $J_{L^+_{5+6}}$, $J_{L^+_4}$ are the corresponding transition density of states, which have a temperature dependence given by

$$J_{\mathrm{i}} = \int_{E^{\mathrm{i}}_{\mathrm{min}}}^{E^{\mathrm{i}}_{\mathrm{max}}} \frac{f_d(E,T_{\mathrm{e}}) - f_p(E,T_{\mathrm{e}})}{k_{\mathrm{i}}(E)}dE \tag{A11}$$

with $\mathrm{i} = X, L^+_{5+6}, L^+_4$.

f_p and f_d are the occupation probabilities of the p and d bands, respectively,

$$f_p(E,T_{\mathrm{e}}) = \frac{1}{1 + \exp\left(\frac{E - \Delta E_{\mathrm{F}}(T_{\mathrm{e}})}{k_{\mathrm{B}}T_{\mathrm{e}}}\right)}, \tag{A12}$$

$$f_d(E,T_{\mathrm{e}}) = \frac{1}{1 + \exp\left(\frac{E - \hbar\omega - \Delta E_{\mathrm{F}}(T_{\mathrm{e}})}{k_{\mathrm{B}}T_{\mathrm{e}}}\right)}, \tag{A13}$$

and

$$k_X(E) = \sqrt{\hbar\omega - E - \hbar\omega_7^X + \frac{m^X_{p\parallel}}{m^X_{d\parallel}}\left(E - \hbar\omega_6^X\right)}, \tag{A14}$$

$$k_L(E) = \sqrt{\hbar\omega - E - \hbar\omega^L_{4^-} - \hbar\omega_0 + \frac{m^L_{p\perp}}{m^L_{d\perp}}\left(E + \hbar\omega^L_{4^-}\right)}, \tag{A15}$$

where $\hbar\omega$ is the photon energy, $\hbar\omega_0$ is $\hbar\omega^L_{5+6}$ or $\hbar\omega^L_{4^+}$, and correspondingly $m^L_{d\perp}$ refers to either the $5+6$ or the 4 d bands.

The Fermi level as a function of electron temperature $E_{\mathrm{F}}(T_{\mathrm{e}})$ is determined starting from the total electron density N_{e} given by

$$N_{\mathrm{e}} = \int_{-\infty}^{\infty} \frac{D(E)dE}{1 + \exp\left(\frac{E - E_{\mathrm{F}}(T_{\mathrm{e}})}{k_{\mathrm{B}}T_{\mathrm{e}}}\right)}. \tag{A16}$$

To determine the change of the Fermi level, we use a limited integration range in Eq. (A16) from $E_{\mathrm{F}}^- = E_{\mathrm{F}}(0) - 10$ eV to

$E_F^+ = E_F(0) + 20$ eV, yielding

$$\int_{E_F^-}^{E_F(0)} D(E)dE = \int_{E_F^-}^{E_F^+} \frac{D(E)dE}{1+\exp\left(\frac{E-E_F(T_e)}{k_B T_e}\right)}, \tag{A17}$$

and the calculated density of states $D(E)$ from Ref. 20.

The integration limits in Eq. (A11) are calculated as in Refs. 22,23 and are near the X point $E_{\min}^X = -20k_B T$, and

$$E_{\max}^X = \hbar\omega_6^X + \left(\hbar\omega - \hbar\omega_6^X - \hbar\omega_7^X\right)\frac{m_{d\parallel}^X}{m_{p\parallel}^X - m_{d\parallel}^X} \tag{A18}$$

if $\hbar\omega \leqslant \hbar\omega_6^X + \hbar\omega_6^7$, or

$$E_{\max}^X = \hbar\omega_6^X + \left(\hbar\omega - \hbar\omega_6^X - \hbar\omega_7^X\right)\frac{m_{d\perp}^X}{m_{p\perp}^X + m_{d\perp}^X} \tag{A19}$$

if $\hbar\omega > \hbar\omega_6^X + \hbar\omega_6^7$. Near the L point, they are

$$E_{\max}^L = -\hbar\omega_{4^-}^L + (\hbar\omega - \hbar\omega_0)\frac{m_{d\parallel}^L}{m_{d\parallel}^L - m_{p\parallel}^L} \tag{A20}$$

if $\hbar\omega \leqslant \hbar\omega_0$, or

$$E_{\max}^L = -\hbar\omega_{4^-}^L + (\hbar\omega - \hbar\omega_0)\frac{m_{d\perp}^L}{m_{d\perp}^L + m_{p\perp}^L} \tag{A21}$$

if $\hbar\omega > \hbar\omega_0$, and

$$E_{\min}^L = -\hbar\omega_{4^-}^L - \frac{\hbar^2}{2m_{p\parallel}^L}\left(\frac{\pi}{4a}\right)^2 + \frac{m_{d\perp}^L}{m_{p\perp}^L + m_{d\perp}^L} \times \left[\frac{\hbar^2}{2}\left(\frac{1}{m_{p\parallel}^L} - \frac{1}{m_{d\parallel}^L}\right)\left(\frac{\pi}{4a}\right)^2 + \hbar\omega - \hbar\omega_0\right]. \tag{A22}$$

The effective mass and band-gap parameters are given in Table I, and the lattice parameter of Au is $a = 0.408$ nm.

To fit the measured ϵ_2^b at 300 K by Johnson and Christy,[19] we use the constants A_X, $A_{L_{5+6}^+}$, $A_{L_4^+}$ as fitting parameters similar to Ref. 22, and obtain $|P_X/P_{L_{5+6}^+}|^2 = 0.26$, $|P_X/P_{L_4^+}|^2 = 0.67$. One also needs to account for a broadening of ϵ_2^b in order to fit the experimentally observed low-energy tail. Instead of following Ref. 22, which used the electron temperature as fit parameter, we consider the effect of the Drude broadening on the transition energy by convoluting ϵ_2^b obtained by Eq. (A10) with the function

$$B(\hbar\omega) = \frac{1.76}{2b\Gamma}\cosh^{-2}\left(\frac{1.76\hbar\omega}{b\Gamma}\right), \tag{A23}$$

which has an integral normalized to 1 and a full width at half-maximum $b\Gamma$ proportional to the Drude broadening. We use

$$\frac{b\Gamma}{5\hbar} = \gamma_0 + \left[b_{\text{e-e}}\left(T_e^2 - T_0^2\right) + b_{\text{e-p}}(T_l - T_0)\right](\hbar\omega_{\text{exc}})^2, \tag{A24}$$

which fits the data of Johnson and Christy[19] at 300 K and accounts for additional broadenings due to electron-electron and electron-phonon scattering processes in the presence of a nonequilibrium electron and lattice temperature on the same ground as in the Drude model.

TABLE I. Au band-structure parameters near the X and L points from Refs. 22 and 30.

∥ Mass	(m_0)	⊥ Mass	(m_0)	Energy	(eV)
$m_{p\parallel}^X$	0.12	$m_{p\perp}^X$	0.22	$\hbar\omega_7^X$	1.77
$m_{d\parallel}^X$	0.91	$m_{d\perp}^X$	0.75	$\hbar\omega_6^X$	1.47
$m_{p\parallel}^L$	0.25	$m_{p\perp}^L$	0.23	$\hbar\omega_{4^+}^L$	2.6
$m_{d\parallel}^{L_4^+}$	0.57	$m_{d\perp}^{L_4^+}$	0.49	$\hbar\omega_{4^-}^L$	0.72
$m_{d\parallel}^{L_{5+6}^+}$	0.7	$m_{d\perp}^{L_{5+6}^+}$	0.63	$\hbar\omega_{5+6}^L$	1.45

APPENDIX B: FWM DYNAMICS FOR LARGE NANOPARTICLES

The SPR of a gold NP in a dielectric surrounding can be described by the dipole approximation for a NP diameters of less than about 40 nm. For larger sizes, retardation effects become significant, resulting in a red-shift of the extinction peak with increasing size. To verify the suitability of our model to describe large NP sizes, we have investigated the dynamics of $\Delta\tilde{\epsilon}$ for a 125-nm gold NP excited and probed at 550 nm (solid lines in Fig. 6). The size of the NP has been estimated by the oscillation period measured in the phase part of the signal P (see previous section). A major difference with respect to the smaller NP sizes investigated is that P has a positive sign. Within our model in the dipole approximation, we can reproduce the position of the absorption cross section (584 nm) obtained including retardation using Mie's theory[31] by reducing the plasma frequency to 7.965 eV. However, when modeling the FWM dynamics (see dashed lines in Fig. 6, the particle-dependent parameters used in these simulations are $G_{\text{e-p}} = 2.5 \times 10^{-5}$ W/K and $g = 1.8$), we can reproduce the overall dynamics only qualitatively. We do correctly simulate the signs of $\Delta\tilde{\epsilon}_R$ and $\Delta\tilde{\epsilon}_I$ and their relative amplitude, with the positive sign of P being a consequence of probing on the blue side of the SPR. However, the delayed rise of $\Delta\tilde{\epsilon}_I$ observed in the experiment is not reproduced by the model. Moreover, the proportionality factor ξ between A (P) and $\Delta\tilde{\epsilon}_I$ ($\Delta\tilde{\epsilon}_R$) does not scale with the NP volume. We attribute these discrepancies to the failure of the dipole approximation.

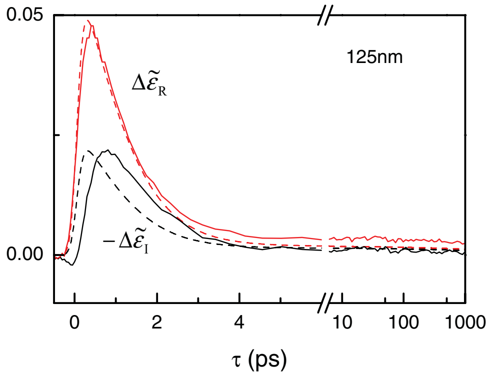

FIG. 6. (Color online) Transient changes of the real ($\Delta\tilde{\epsilon}_R$) (red) and imaginary parts ($\Delta\tilde{\epsilon}_I$) (black) of the dielectric function of a single 125-nm gold nanoparticle. Pump (probe) fluence is 0.65 J/m^2 (0.05 J/m^2). Dashed lines are calculations as described in the text.

APPENDIX C: COHERENT PHONON OSCILLATIONS

The visibility of coherent phonon oscillations in $\Delta\tilde{\epsilon}_R$ is described by the change of the plasma frequency due to the changing volume of the NP during the breathing oscillation, driven by the nonadiabatic thermal expansion of the NP during the thermalization with the lattice in the first picoseconds:

$$\omega_p = \frac{\omega_{p0}}{\sqrt{\overline{\alpha}(T_l - T_0)\left[1 + C\cos\left(\frac{2\pi\tau}{T_o} + \phi\right)e^{-\frac{\tau}{T_d}}\right] + 1}} \tag{C1}$$

with the bulk volumetric expansion coefficient $\overline{\alpha} = 4.5 \times 10^{-5}\ \mathrm{K}^{-1}$. To fit the oscillations measured on the 38-nm NP shown in the inset of Fig. 2, we used $C = 0.75$, $T_o = 12.8$ ps, $T_d = 80$ ps, and $\phi = -3.33$. The oscillation period is the period of the fundamental breathing mode in a spherically symmetric NP,[11] from which we deduce a particle diameter of 38 nm following the values in Ref. 13. The quantitative agreement of the oscillation amplitude using a factor of $C = 0.75$ is supporting this interpretation since for an instantaneous lattice heating, we would expect $C = 1$, and for a realistic heating time of a few picoseconds, this value is expected to be somewhat reduced.

APPENDIX D: VALIDITY OF THE ENERGY TRANSFER IN THE TWO-TEMPERATURE MODEL

To verify the validity of the two-temperature model, we have investigated the dependence of the energy transfer rate from the electrons to the lattice $\Delta u/\Delta\tau$ on the difference between the electron and lattice temperature $T_e - T_l$. All these quantities can be retrieved directly from the FWM signal when we assume that the total amplitude $E_{\mathrm{FWM}} = \sqrt{A^2 + P^2}$ of the field can be approximated as

$$E_{\mathrm{FWM}} = a\left(T_e^2 - T_0^2\right) + b(T_l - T_0). \tag{D1}$$

The electron and lattice temperature can then be determined from the FWM amplitude considering the energy conservation within the NP, which holds for delay times much shorter than the typical thermalization time with the environment of some 100 ps:

$$u = \frac{\gamma T_e}{2}\left(T_e^2 - T_0^2\right) + C_l(T_l - T_0) \tag{D2}$$

resulting in

$$T_e = \sqrt{\frac{E_{\mathrm{FWM}} - bu/C_l}{a - b\gamma/(2C_l)} + T_0^2} \tag{D3}$$

and

$$T_l = \frac{1}{C_l}\left(u - \frac{\gamma}{2}\left(T_e^2 - T_0^2\right)\right) + T_0. \tag{D4}$$

The values of a and b can be found by comparing the dynamics of T_e calculated with the two-temperature model and the value of the electron temperature obtained by Eq. (D3). The value of the energy u has been estimated from the incident energy flux and the nanoparticle absorption cross section. Once the values of a and b are determined, the energy transfer rate can be calculated in a finite difference scheme between the ith and $(i+1)$th points of the measured FWM amplitude dynamics:

$$\frac{\Delta u}{\Delta\tau} = \frac{\gamma}{2}\frac{T_{e_{i+1}}^2 - T_{e_i}^2}{\tau_{i+1} - \tau_i}. \tag{D5}$$

The values of $-\Delta u/\Delta\tau$ as a function of the electron-lattice temperature difference $T_e - T_l$ are shown in Fig. 7 for a 38-nm NP at an excitation intensity of 0.65 J/m^2 at 550 nm and for a 20-nm NP an an excitation intensity of 0.60 and 1.3 J/m^2 at 550 nm. The data refer to a delay range of 0.7–5 ps, i.e., in the cooling regime of the electron gas. Within the experimental errors, the energy transfer rate depends linearly on $T_e - T_l$, consistent with the energy transfer equation used in the two-temperature model. The linear coefficient does not depend on the excitation intensity and is given by the electron-phonon coupling constant $G_{\text{e-p}}$.

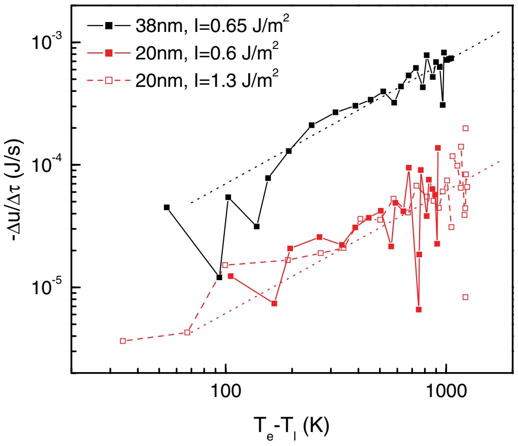

FIG. 7. (Color online) Electron energy transfer rate as a function of $T_e - T_l$ for 38-nm NP with excitation intensity of 0.65 J/m^2 (black squares) at 550 nm and for a 20-nm NP with excitation intensity of 0.60 (red solid squares) and 1.3 J/m^2 (red open squares) at 550 nm. The dotted lines show a linear dependence with coefficients proportional to the electron-phonon coupling constant $G_{\text{e-p}}$.

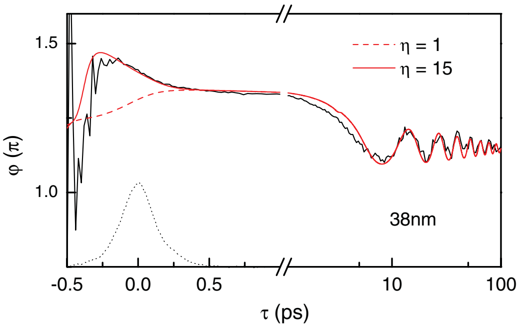

FIG. 8. (Color online) Transient change of the phase of $\Delta\tilde{\epsilon}$ from the ratio between its imaginary and real parts, measured on the 38-nm NP for an excitation and detection wavelength of 550 nm. Red dashed line is a simulation using $\eta = 1$ in the shift of the plasma frequency [Eq. (E1)], while the solid line uses $\eta = 15$, as indicated. The black dotted line is the pulse intensity autocorrelation measured in the experiment.

APPENDIX E: RATIOMETRIC DETECTION OF THE SIGNAL PHASE

An intrinsic ratiometric way to represent the measured FWM signal is to plot the phase φ of $\Delta\tilde{\epsilon} = |\Delta\tilde{\epsilon}| \exp(i\varphi)$ from the ratio between its imaginary and real parts, as shown in Fig. 8 for the 38-nm NP at 550 nm. Notably, the visibility of the coherent phonon oscillations is improved in φ since it is independent of decay dynamics common to real and imaginary parts of $\Delta\tilde{\epsilon}$, while a frequency shift in the SPR changes φ.

Our simulations include the effect of the change in the plasma frequency from the excess electron density calculated using

$$\omega_{\mathrm{p}} = \omega_{\mathrm{p}}^{0} \sqrt{\left(1 + \eta \frac{n_X^{\mathrm{nth}} + n_L^{\mathrm{nth}}}{n_{\mathrm{e}}}\right)}. \qquad \text{(E1)}$$

The presence of an excess electron density equal to the density of holes generated via the interband transitions is corresponding to $\eta = 1$. All simulations of the dynamics of $\Delta\tilde{\epsilon}_{\mathrm{I}}$ and $\Delta\tilde{\epsilon}_{\mathrm{R}}$ shown previously are performed using $\eta = 1$. We notice in Fig. 8 that the initial phase dynamics on the time scale of the excess density lifetime (i.e., for $\tau \leqslant 0.5$ ps) shows a significant discrepancy to the simulation for $\eta = 1$, which disappears for $\eta = 15$ (red solid line in Fig. 8). Possible mechanisms leading to the larger effective η describing the measurements are the hole density, which was neglected in the plasma frequency, and the localization of the created carriers in specific points of the Brillouin zone, having effective masses deviating from the average effective mass m_0 used in the definition of the plasma frequency.

In the simulations of $\Delta\tilde{\epsilon}_{\mathrm{I}}$ and $\Delta\tilde{\epsilon}_{\mathrm{R}}$ at 550 nm shown in Fig. 9, the effect of η manifests as a small shift of the initial rise, in opposite directions for the real and imaginary parts of $\Delta\tilde{\epsilon}$: increasing η shifts $\Delta\tilde{\epsilon}_{\mathrm{I}}$ toward earlier times and $\Delta\tilde{\epsilon}_{\mathrm{R}}$ toward later times. This effect, however, does not modify significantly the initial rise time, which instead is determined by the d-state Auger thermalization time $\tau_{\mathrm{b}} = 70$ fs. To elucidate this point, we show also the effect of changing τ_{b} to 500 fs (equal to the free-electron thermalization time constant τ_{f}) for both $\eta = 1$ and 15. A longer τ_{b} clearly shows as a slower rise time dynamics, which can not be compensated by changing η and does not agree with the measurements.

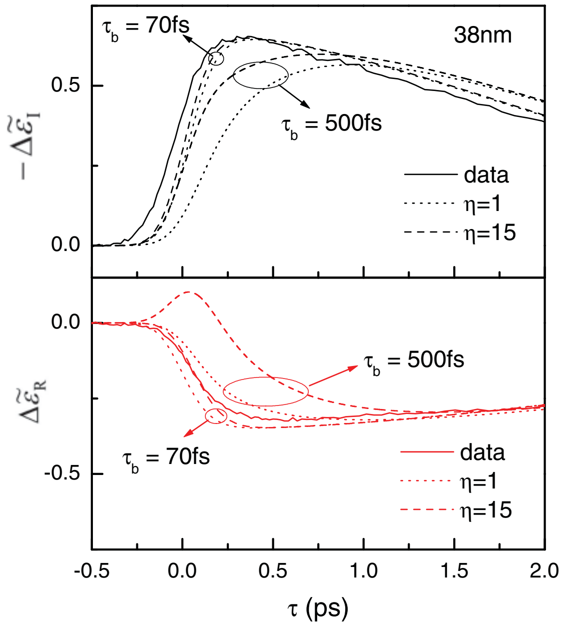

FIG. 9. (Color online) Transient change of the real and imaginary parts of $\Delta\tilde{\epsilon}$ measured on the 38-nm NP for an excitation and detection wavelength of 550 nm, with simulations for $\eta = 1$ (dotted lines) and $\eta = 15$ (dashed lines) and for $\tau_{\mathrm{b}} = 70$ or 500 fs as indicated.

---

*borrip@cardiff.ac.uk

[1] P. K. Jain, K. S. Lee, I. H. El-Sayed, and M. A. El-Sayed, J. Phys. Chem. B **110**, 7238 (2006).

[2] S. Berciaud, L. Cognet, P. Tamarat, and B. Lounis, Nano Lett. **5**, 515 (2005).

[3] O. L. Muskens, P. Billaud, M. Broyer, N. Del Fatti, and F. Vallée, Phys. Rev. B **78**, 205410 (2008).

[4] D. Boyer, P. Tamarat, A. Maali, B. Lounis, and M. Orrit, Science **297**, 1160 (2002).

[5] M. A. van Dijk, A. L. Tchebotareva, M. Orrit, M. Lippitz, S. Berciaud, D. Lasne, L. Cognet, and B. Lounis, Phys. Chem. Chem. Phys. **8**, 3486 (2006).

[6] K. Lindfors, T. Kalkbrenner, P. Stoller, and V. Sandoghdar, Phys. Rev. Lett. **93**, 037401 (2004).

[7] M. Lippitz, M. vanDijk, and M. Orrit, Nano Lett. **5**, 799 (2005).

[8] O. Schwartz and D. Oron, Nano Lett. **9**, 4093 (2009).

[9] F. Masia, W. Langbein, P. Watson, and P. Borri, Opt. Lett. **34**, 1816 (2009).

[10] C. Voisin, D. Christofilos, P. A. Loukakos, N. Del Fatti, F. Vallée, J. Lermé, M. Gaudry, E. Cottancin, M. Pellarin, and M. Broyer, Phys. Rev. B **69**, 195416 (2004).

[11] G. V. Hartland, Chem. Rev. **111**, 3858 (2011).

[12] O. L. Muskens, N. Del Fatti, and F. Vallée, Nano Lett. **6**, 552 (2006).

[13] M. A. van Dijk, M. Lippitz, and M. Orrit, Phys. Rev. Lett. **95**, 267406 (2005).

[14] M. A. van Dijk, M. Lippitz, D. Stolwijk, and M. Orrit, Opt. Express **15**, 2273 (2007).

[15] Van Dijk *et al.* (Ref. 14) detected the transmission interferometrically using a reference field to distinguish changes in amplitude and phase. However, their setup utilizes probe and reference pulses traveling through the sample separated in time by 10 ps, which resulted in the measurement of the 10-ps difference in the pump-induced change of the field. This quantity is only indirectly related to the change in the NP complex dielectric function, which could not be extracted from their data.

[16] P. Borri, W. Langbein, J. Mørk, and J. M. Hvam, Opt. Commun. **169**, 317 (1999).

[17] V. Cesari, P. Borri, M. Rossetti, A. Fiore, and W. Langbein, IEEE J. Quantum Electron. **45**, 579 (2009).

[18] C. Voisin, N. Del Fatti, D. Christofilos, and F. Vallee, J. Phys. Chem. B **105**, 2264 (2001).

[19] P. B. Johnson and R. W. Christy, Phys. Rev. B **6**, 4370 (1972).

[20] Z. Lin, L. V. Zhigilei, and V. Celli, Phys. Rev. B **77**, 075133 (2008).

[21] J. B. Smith and H. Ehrenreich, Phys. Rev. B **25**, 923 (1982).

[22] M. Guerrisi, R. Rosei, and P. Winsemius, Phys. Rev. B **12**, 557 (1975).

[23] R. Rosei, Phys. Rev. B **10**, 474 (1974).

[24] To represent the measurement conditions in the detection, the calculated $\tilde{\epsilon}$ is convoluted with the pulse intensity Gaussian profile.

[25] E. Knoesel, A. Hotzel, and M. Wolf, Phys. Rev. B **57**, 12812 (1998).

[26] A. Arbouet, C. Voisin, D. Christofilos, P. Langot, N. Del Fatti, F. Vallée, J. Lerme, G. Celep, E. Cottancin, M. Gaudry, M. Pellarin, M. Broyer, M. Maillard, M. P. Pileni, and M. Treguer, Phys. Rev. Lett. **90**, 177401 (2003).

[27] C. Sönnichsen, B. M. Reinhard, J. Liphardt, and A. P. Alivisatos, Nat. Biotech. **23**, 741 (2005).

[28] Y. Hamanaka, J. Kuwabata, I. Tanahashi, S. Omi, and A. Nakamura, Phys. Rev. B **63**, 104302 (2001).

[29] M. Rashidi-Huyeh and B. Palpant, J. Appl. Phys. **96**, 4475 (2004).

[30] N. E. Christensen and B. O. Seraphin, Phys. Rev. B **4**, 3321 (1971).

[31] M. van Dijk, Ph.D. thesis, Leiden University, 2007.